



Integration of electrically detected magnetic resonance on a chip (EDMRoC) with charge pumping for low-cost and sensitive defect characterization in SiC MOSFETs

Jan Lettens^{1,2}, Marina Avramenko², Ilias Vandevenne¹, Anh Chu^{3,4}, Philipp Hengel^{3,4}, Michal Kern^{3,4},
5 Jens Anders^{3,4}, Peter Moens², Etienne Goovaerts¹, Sofie Cambré¹

¹Department of Physics, University of Antwerp, Antwerp, 2610, Belgium

²onsemi, Westerring 15, Oudenaarde, 9700, Belgium

³Institute of Smart Sensors, Universität Stuttgart Stuttgart 70569, Germany

⁴Center for integrated Science and Technology (IQST), Stuttgart, 70569, Germany

10 *Correspondence to:* Sofie Cambré (sofie.cambre@uantwerpen.be)

Abstract. Integration of microwave sources and detection circuits has led to the design of very compact electron paramagnetic resonance (EPR) instruments, so-called EPR on-a-chip (EPRoC). As recently demonstrated, this approach also offers opportunities for electrical detection of magnetic resonance (EDMR), a variant of EPR in which the magnetic resonance effect is detected via changes in the electrical properties of materials or devices. Here, we report the demonstration
15 of EDMRoC on lateral SiC MOSFETs under charge pumping (CP) conditions. The detected CP current gives direct access to microscopic information about the recombination centers within the transistor gate inversion region under the gate dielectric. Efficient and selective microwave excitation of the region of interest of the device can be obtained by only modest modifications to both the MOSFET and the EPRoC electronic board. A comparative study between EDMRoC and a traditional resonant cavity configuration reveals comparable signal-to-noise ratios for CP-detected EDMR spectra. In
20 addition to space- and cost-efficiency, EDMRoC offers alternative detection modes with scanning and modulation of the microwave frequency, as well as potentially easier sample mounting and exchange. We end with a discussion of the advantages, limitations, and perspectives of the EDMRoC set-up compared to EDMR in a conventional EPR spectrometer.

1 Introduction

Electrical detection of magnetic resonance (EDMR), probing electron paramagnetic resonance (EPR) via changes in
25 electrical properties due to spin-dependent processes, has become a method of choice for microscopic characterization of performance-limiting defects in semiconductor materials and devices.(Boehme and Malissa, 2017) The latter includes 2-terminal devices such as diodes and solar cells,(Akhtar et al., 2015; Anders et al., 2018; Boehme and Malissa, 2017; Lepine, 1972; Li et al., 2004; Malissa et al., 2014; Rong et al., 1991; Tedlla et al., 2015) but also more complex devices such as metal-oxide-semiconductor field-effect transistors (MOSFETs).(Ashton et al., 2019; Bittel et al., 2011; Cochrane et al.,
30 2010; Cottom et al., 2018; Umeda et al., 2011, 2018, 2019) Recombination centers in the transistor channel area are directly



related to performance limitations and degradation during operation in these devices, in particular in the technologically important case of silicon carbide (SiC) MOSFETs.(Allerstam et al., 2007; Bathen et al., 2022; Harada et al., 2002; Wang et al., 2023) Therefore, EDMR spectroscopy has been applied early on for defect characterization using different detection schemes based on changes in transimpedance between different terminals of the transistor.(Aichinger and Lenahan, 2012; 35 Ashton et al., 2019; Cochrane et al., 2010, 2012; Cottom et al., 2018; Kagoyama et al., 2019; Sometani et al., 2023; Umeda et al., 2011, 2018, 2019) However, in our experiments, we apply the spin-dependent charge pumping EDMR scheme (SDCP or CP-EDMR) as first demonstrated by (Bittel et al., 2011), which is based on the well-established charge pumping (CP) method for transistor characterization.(Van den bosch et al., 1991; Brugler and Jespers, 1969; Djezzar, 2023; Groeseneken et al., 1984; Lettens et al., 2023; Okamoto et al., 2008) The CP current monitored in this scheme is induced by a rectification 40 effect between the base and source (and/or drain) terminals under excitation of the gate by a voltage periodically alternating between two voltage levels. These two levels are chosen such that alternatively either electrons or holes are attracted to and extracted from the transistor channel region, and recombination occurs at trapping sites. Albeit more intricate, the CP version of EDMR can offer a direct correlation with the results of CP characterization.(Aichinger et al., 2013; Anders et al., 2020; Bittel et al., 2011; Cochrane et al., 2013; Gruber et al., 2014, 2018) It potentially also offers higher selectivity in several 45 ways: (i) by the choice of applied voltage levels that may be energetically aligned to specific defect levels, and (ii) by variation of other CP-excitation parameters (frequency, rise/fall times, duty cycle) which help to discriminate between traps with different temporal characteristics and/or spatial distribution. Although EDMR has been frequently applied to investigate defects in MOSFETS, the requirement of (expensive) dedicated equipment prevents it from being routinely used. Therefore, a non-resonant EDMR application, replacing the microwave (MW) resonator of the conventional EDMR by a non-resonant 50 antenna has been successfully applied to measure frequency-swept and rapid scan EDMR spectra.(McCrory et al., 2019)

In recent years, developments in MW electronics have led to so-called EPR-on-a-chip (EPRoC), – a single-board EPR set-up with an integrated MW oscillator chip –, which allows for extremely compact and low-cost EPR instrumentation.(Anders et al., 2012; Yalcin and Boero, 2008) In conventional EPR experiments, the sample is inserted in a high-Q MW resonator 55 providing standing waves with high amplitudes of the magnetic field component and minimal electrical field components at the sample position, for high detection sensitivity and low dissipation losses, respectively (see Fig. 1(d) for a photograph of a typical setup). Often, the insertion of an electronic device in a resonator is not straightforward, considering both the specific requirements in size and geometry and the presence of metallic conductors interfering with the MWs, as discussed in detail in (Segantini et al., 2023). On the contrary, in EPRoC, the MWs are generated using a voltage-controlled oscillator (VCO) 60 integrated using commercial silicon chip fabrication technologies. The coils in the VCO serve both for generation of the near-field MW fields as well as for inductive detection of spin signals. Samples are positioned in the proximity field of this MW chip (see comparison in Fig. 5 of (Segantini et al., 2023)). This was shown to be versatile, with a wide range of possible MW frequencies (up to a first harmonic oscillation frequency of 263 GHz,(Chu et al., 2023) even several frequencies combined as well as their higher-order harmonics (Handwerker et al., 2016; Matheoud et al., 2017)) and it allows frequency



65 scanning/modulation (replacing conventional static magnetic field scanning/modulation). Moreover, the MW chip, which
can be adapted in size and shape, is very well suited for excitation of thin planar samples. This was very recently exploited
by (Segantini et al., 2023) in a demonstration of EDMR-on-a-chip (EDMRoC) in a thin film a-Si:H solar cell, using the
EPRoC MW source and detecting EDMR via the change in conductivity of the photovoltaic active layer under forward bias.

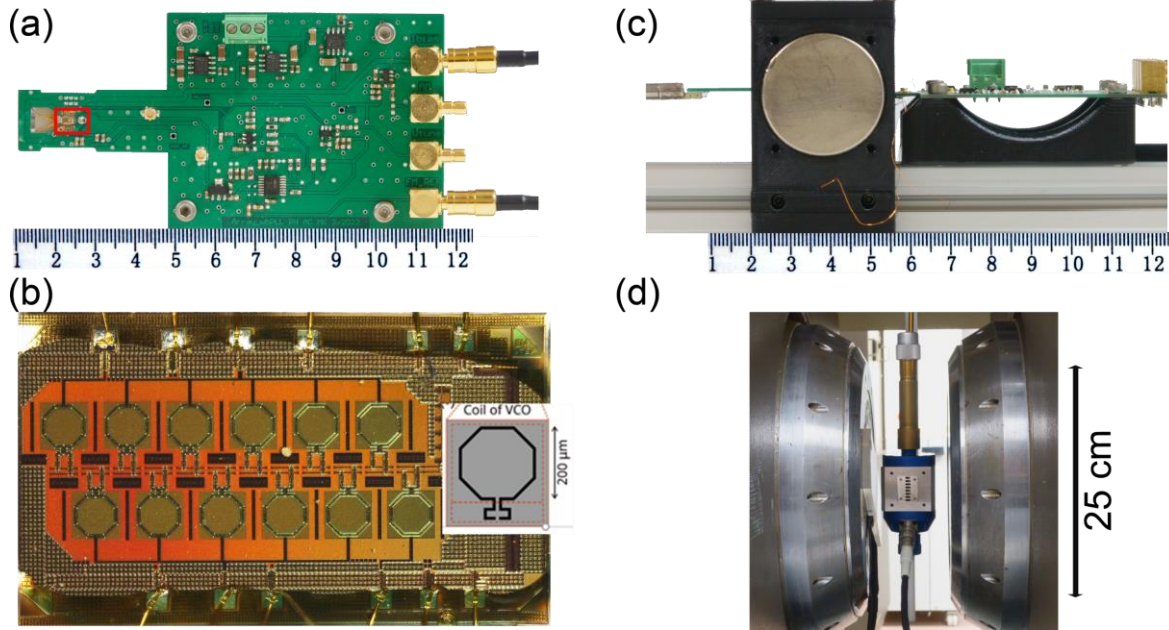
70 Here, we extend EDMRoC spectroscopy to measurements of EDMR on lateral SiC MOSFETs using the powerful CP
detection scheme mentioned above. The MOSFET chips are well matched to the dimensions of the EPR chip and mounted in
a way appropriate for measurements either in the EDMRoC approach using the EPRoC MW source, or in the resonator of
the X-band EPR spectrometer. As a result, direct and quantitative comparisons were obtained, showing a signal to noise ratio
(SNR) comparable in EDMRoC with the optimized conventional experiment. Results will be shown with varying
75 instrumental parameters and using different scanning/modulation methods. Finally, a compact set-up using a permanent
magnet is demonstrated.

2. Results and Discussion

2.1. Design of EDMRoC for SiC MOSFETs

2.1.1. Microwave Generation

80 The basis of our EDMRoC experiments is the printed circuit board (PCB) shown in Fig. 1(a) and Fig. 1(b), providing an
integrated MW source. It is very similar to the one applied in (Segantini et al., 2023) however without the transimpedance
amplifier (TIA). As discussed below, we rather use the external TIA employed for EDMR in our conventional EPR setup
because of the specific requirements for detection via CP. On this main board, MWs are generated by an application-specific
integrated circuit (ASIC) carrying an injection-locked array of voltage-controlled oscillators (VCO) with variable frequency
85 in a range of width ≈ 2.5 GHz centered around the design frequency of 14 GHz. The VCO-array oscillation frequency is
divided on-chip and made available off-chip by a ratio of 32. This allows for a custom-made phase-locked loop (PLL) on the
PCB to lock the divided frequency to the output frequency of a radio frequency (RF) generator (Rhode&Schwarz
SMC100A). The EPR chip (see Fig. 1(b)), with two rows of six 200 μm octagonal coils each, placed apart 300 μm center-to-
center within one row and 425 μm center-to-center in between the two rows, generates MWs linearly polarized with the
90 magnetic field \mathbf{B}_1 perpendicular to the surface, quite rapidly decreasing with distance from the chip surface. The generated
MW power can be adjusted and monitored via the summed control current I_{BIAS} (17.5-300 mA), (Künstner et al., 2021) with a
threshold current $I_{\text{BIAS}} \cong 17.5$ mA and a smooth and continuous behavior up till the highest current values $I_{\text{BIAS}} \cong 300$ mA
(see Appendix **Fig. A1(b)**). The quantitative comparison with MW powers supplied in the resonant cavity set-up will be
discussed below (see **Fig. 3** and **Appendix A and B**).



95

100

Figure 1: a) Photograph of the EDMRoC PCB holding the ASIC with MW source circuitry (indicated by the red rectangle). b) Zoomed-in photograph of the MW ASIC with VCOs containing 12 octagonal coils and schematic drawing of one octagonal coil of one VCO. c) side-view of the EDMRoC PCB (right side), the sample PCB with connector (left side) and a permanent magnet centred on the sample which is mounted on a rail for easy device accessibility and mounting. d) Photograph of the resonator for conventional EDMR

105

In the conventional EDMR experiment, the MWs generated in the bridge of a standard X-band spectrometer (Bruker Elexsys E500) are delivered into a high-Q cylindrical TE₀₁₁ resonator (ER4122SHQE, Fig. 1(d)). The sample is positioned in the center of the resonator where the MW magnetic field is maximum, optimizing the magnetic resonance effect, while there is a minimum in the MW electric field, minimizing detrimental losses. These losses are critically dependent on the precise positioning of such samples, with their metallic and semiconductor parts, and lead to a decrease of the resonator Q-factor, hence of the amplitude of the MWs, and therefore also of the detection efficiency. The resonator is mounted in such a way that the magnetic field component of the MWs is perpendicular to the externally applied magnetic field, provided by a variable electromagnet.

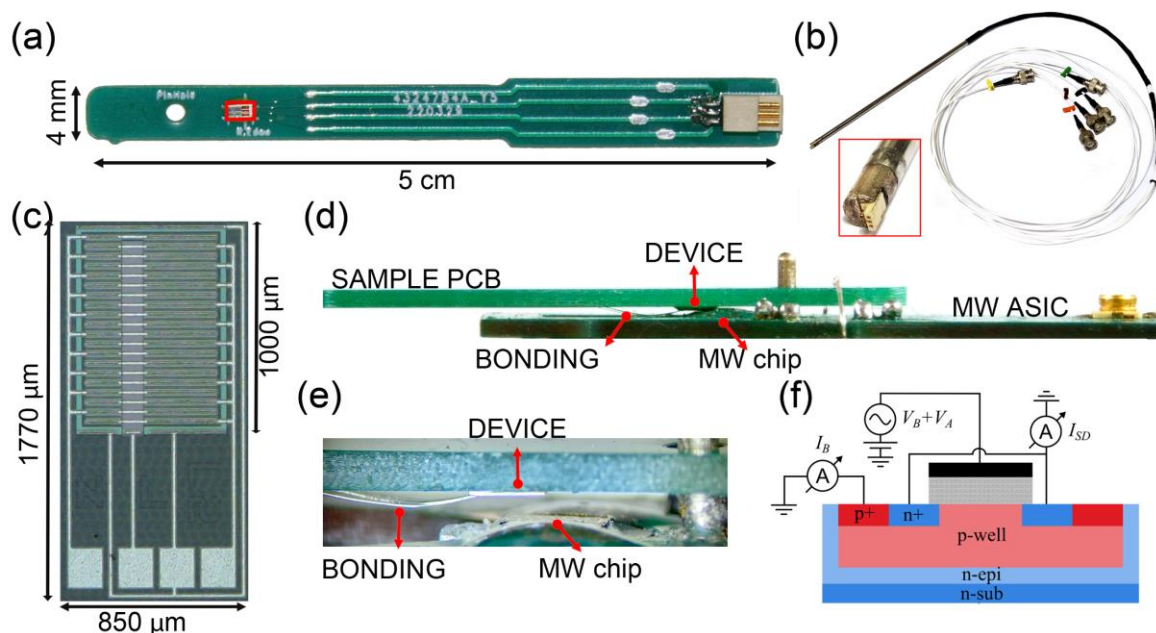
115

2.1.2. The MOSFET device

Lateral n-channel SiC MOSFETs have been produced with a total gate width of 12.1 mm (19 fingers of each $W = 635 \mu\text{m}$) and channel length $L = 2 \mu\text{m}$. The layout and cross-section are pictured in Fig. 2(c) and Fig. 2(f). The gate oxide was grown with thermal oxidation in a dry (O_2) ambient to a thickness of 40 nm. All devices were made on highly nitrogen doped, 4° off-axis, 4H-SiC substrates on which $10 \mu\text{m}$ SiC was epitaxially grown with a nitrogen doping concentration of 10^{16}cm^{-3} . P-type doping for the well was done by aluminum implantation to a depth of $1 \mu\text{m}$ and a surface concentration of 10^{17}cm^{-3} . The regions above the transistor junction are free from metallization and the only conductive layer is a $0.5 \mu\text{m}$ layer of n+



poly-Si (with specific sheet resistivity of $\sim 300\text{--}400\Omega/\text{square}$) forming the gate electrode and sufficiently separated from the metallic stripes forming the other electrodes. This allows for efficient penetration of the MWs to the relevant region.



120 **Figure 2:** (a) The device (marked by a red rectangle) is mounted on a dedicated sample PCB providing an alignment pinhole and 4
metallized tracks between contact paths and a 6-pin connector. (b) Connecting tube with an identical 6-pin counter-connector
(zoomed-in version in the red box) to a set of coax cables for shielded electrical connection in the different setups. (c) Photograph
of the MOSFET layout, with a width of $635\ \mu\text{m}$, a gate length of $2\ \mu\text{m}$ and 19 fingers, and dimensions $850 \times 1770\ \mu\text{m}^2$, and an
active device area of $635 \times 1000\ \mu\text{m}^2$. The 4 contact pads are connected to the MOSFET source, drain, gate and body. (d) sample
125 PCB mounted on top of MW ASIC using the alignment pin with device, bonding wires, and MW chip. (e) Zoom-in showing the
overlap between device and MW chip and the free space on the MW PCB for the bonding wires. Here, the device PCB is slightly
lifted while for actual measurements it is brought in close contact with the MW chip (as in panel (d)). (f) Schematic MOSFET
cross-section and electrical scheme for CP.

2.1.3. Mounting of the MOSFET device

130 The studied devices were adapted to the constraints of both the EDMRoC and the conventional EDMR experiments. They
are mounted on a sample holder (see Fig. 2(a)) consisting of a PCB which fits within the diameter of the sample room in the
EPR resonator and provides practical mechanical and electrical connection to a long tube accessory that contains the
shielded coaxial cables (see Fig. 2(b)) for device biasing as well as for CP excitation and detection. To minimize stray fields,
magnetic materials were avoided as much as possible in the sample PCB, in particular in its metallization bonding paths
135 (PCB Solutions; lead-free HASL metallization). Even so, the latter were kept at a distance ($> 4\ \text{mm}$) from the studied device
to avoid any effect of residual ferromagnetism. The dimensions of the SiC MOSFET chip ($850 \times 1770\ \mu\text{m}^2$, see Fig. 2(c))
are adapted to the available space between the contact wires on the MW chip (Fig. 1(b)). Also, the active area of the
transistor of $635 \times 1000\ \mu\text{m}^2$ (Fig. 2(c)) is fitting well to that of the EDMRoC MW chip. Reference points for device position



and alignment hole (*versus* the matching alignment pin on the main board, see Fig. 1) allow for precise relative positioning
of MOSFET and MW chip in the EDMRoC experiments, as shown in Fig. 2(d) and schematically illustrated in Fig. D1 in
appendix D. The bonding wires connecting the device to the sample PCB extend above the chip with risk of damage when
the MOSFET is brought close to the MW chip. For this reason, the four contact pads were placed on one end of the chip at
maximum distance from the active area (Fig. 2c). Correspondingly, a pentagonal hole was prepared on the main board next
to the MW chip (see Fig. 1(a)), offering free space for the bonding wires that would otherwise hit the board, as illustrated by
Fig. 2(d) and Fig. 2e.

2.1.4. Charge Pumping and EDMR Detection

To generate the CP effect, the sum of a DC voltage V_B and a square signal is applied to the gate, using a DC power supply
($\pm 20V$; HP E3615A) and an arbitrary waveform generator (HP 33120A). As such the gate voltage alternates between V_B and
 $V_A + V_B$ at a chosen frequency (f_{CP}). As a result, DC currents are measured on all terminals of the MOSFET except on the
gate, denoted by corresponding subscripts (see Fig. 2(f); SD for source-drain and B for bulk). Note that in the present
experiments, the source and drain are electrically shorted, and the substrate is not connected, thus the CP current is measured
via the bulk contact. Throughout the manuscript, we will present results for the following CP excitation parameters
optimized for an easy observation of the EDMR spectrum: amplitude $V_A = 10$ V, frequency $f_{CP} = 113$ kHz, and base voltage
value $V_B = -10.5$ V (see further, Fig. 3a for the CP current as a function of V_B).

The recombination current detected in the CP experiment depends on the spin state of the carrier pairs involved in
recombination processes in the transistor channel region. (Boehme and Malissa, 2017; Kaplan et al., 1978; Lepine, 1972;
Segantini et al., 2023) The spins can be flipped by absorption of MW quanta if the condition of magnetic resonance is
fulfilled, *i.e.* when $h\nu = g\mu_B B_0$ (with h for Planck's constant, ν the MW frequency, g the Landé g -factor, μ_B the Bohr
magneton, and B_0 the applied static magnetic field).

2.1.5. Scanning/Modulation Techniques and Signal Treatment

In most EPR measurements, the static field B_0 is generated by an electromagnet (Fig. 1(d)) which is scanned to detect the
resonance, as the MW frequency is set by the high-Q MW resonator and thus cannot be varied. In the EDMRoC
configuration, we are free to scan either the applied magnetic field B_0 (at fixed MW frequency ν) or the MW frequency ν (at
fixed B_0). Indeed, in the absence of a high-Q resonator there is no constraint on frequency. This also reflects onto the applied
modulation techniques: in the conventional set-up the standard approach is B_0 -field modulation (BM) combined with phase-
sensitive detection to achieve high signal-to-noise ratios (SNRs), which at the same time leads to first-derivative line shapes
in the recorded spectra (see examples further in Fig. 3 and Fig. 4). On the contrary, magnetic field modulation is not
implemented in our EDMRoC set-up and replaced by frequency modulation (FM), *i.e.* a sinusoidal modulation of the MW
frequency ν , providing at least equivalent SNRs as will be shown below. Both the in-phase and quadrature components to



170 the signal arising from the phase-sensitive detection are detected. However, in the present series of measurements only the in-phase contribution will be considered as no significant phase shifts were found.

The final steps in the signal generation and treatment are common to both approaches, allowing as much as possible a direct comparison of signal strengths. The external TIA (SR570 – low noise current preamplifier from Stanford Research Systems) provides flexible low-pass filtering blocking the crosstalk induced by the excitation (at 113 kHz) of the CP current, while
175 passing the AC signal induced on the CP-current by the low-frequency modulation (730 Hz, in either BM or FM). The modulated component in the TIA output is then selectively detected by the internal lock-in amplifier (LIA; the so-called Signal Processing Unit) of the EPR spectrometer. Throughout these measurements all settings of the external TIA and LIA were kept constant.

2.2. Comparison of Conventional EDMR and EDMRoC

180 2.2.1. The EDMR spectra and their MW power dependence

CP-detected EDMR spectra recorded for the same device using the field-swept mode are presented in **Fig. 3**, either in the resonator configuration with BM (**Fig. 3(c)**) or in the EDMRoC setup with FM (**Fig. 3(d)**). Single scan measurements with total integration time of 3 min are shown to illustrate the comparable SNR obtained in both cases. This requires a more detailed evaluation, since direct comparison of the MW power delivered in the region of interest in the MOSFET, *i.e.* in the
185 transistor junction areas, is not evident as the spatial distributions of magnetic and electric field components are very different in both approaches.

In the cylindrical SHQ resonator the sample is inserted in the central position where the B_1 field component (MWs) is maximum, for strongest excitation of magnetic resonance. This is also the best region for homogeneity of B_1 . All parts of the sample and its holder are immersed in the MW field, which requires attention for the use of low-loss materials, as mentioned
190 above. Favorably, the E_1 field component, relevant for losses in dielectric and conductive materials, is smallest in the sample area, in the middle of the resonator. Accurate positioning is thus critical for typical EDMR samples as insertion of a MOSFET sample with its highly conductive semiconductor layers, metallization and bonding wires introduces losses and may induce local distortion of the mode depending on sample position and orientation. Indeed, the unloaded value of the quality factor Q is reduced from nearly 16700 to about 6560 (see curves for empty and loaded resonator in Appendix E, **Fig. E1**). This Q-value is still high compared to other resonators, offering the best possible SNR for in-resonator experiments and thus the golden standard for comparison with the EDMRoC results. From this Q-factor and the specific resonator conversion factor $C' = 0.23 \text{ mTMHz}^{1/2} \text{ W}^{-1/2}$ (Anon, 2024; Eaton et al., 2010a) one can estimate values of $B_1 \cong 30 \text{ } \mu\text{T}$ and $84 \text{ } \mu\text{T}$ for the MW power levels of 25 mW and 200 mW, corresponding to the measurements depicted in **Fig. 3a**.

In EDMRoC, on the other hand, the near-field MW magnetic field in the proximity of the coil array is impinging on the front
200 side of the MOSFET device. The interaction with the sample is limited to the most relevant part of the device and this avoids interaction with the chip's substrate as well as with components of the sample holder. Very recently, both a calculation and



an experimental mapping were performed of the MW field emitted by this specific EPR chip.(Künstner et al., 2024) The EPR signal of a 15 μm thick a-Si film was measured to rapidly decrease with distance, dropping below 20% at 60 μm of the MW chip surface, which shows that variations in the vertical position of the sample critically affect the impinging MW intensity. Also, in a horizontal plane above the chip surface the generated MW field presents important inhomogeneities. From a field simulation, recently performed for this specific VCO device,(Künstner et al., 2024) we include relevant results calculated at the chip's surface as well as in a plane 25 μm above it (see Appendix G, Fig. G1, left and right panel, respectively). This figure illustrates that the B_1 component perpendicular to the plane ($B_{1,z}$) is large in the areas above the coil and becomes quite constant within that area. However, this represents less than half of the chip's surface. It is worth noting here that transition probabilities in magnetic resonance are quadratically dependent on the B_1 components, which tends to emphasize the effects of inhomogeneity. This simulation was performed for a bias current of approximately 3 mA per coil, corresponding to $I_{BIAS} = 40$ mA. Based on the analysis of rapid-scan EPR measurements (Künstner et al., 2021) a B_1 field just above the coil was derived close to 30 μT , interestingly of the same order of magnitude as derived earlier for the case of the resonator. It should be noted that this B_1 value is an underestimation of the one at the coil center, because of the relatively large sample used in these rapid-scan EPR experiments in addition to other uncertainties in the analysis of the EPRoC circuit.

For an experimental comparison of the MW power on the sample, considering the qualitative differences in B_1 field properties, we studied the saturation of both EDMR signals. Figure 3b shows the signal intensities from resonator EDMR and from EDMRoC as a function of increasing MW power. In the first case, it is straightforward to choose the calibrated power delivered by the MW bridge. In the latter, the power emitted by the VCO can be adjusted by setting I_{BIAS} , but the relationship deviates from linearity. As described in Appendix A, Fig. A1, we establish a linear scale, albeit not absolutely calibrated, for emitted power in EDMRoC based on the electronic circuit simulation of the VCO at increasing bias current I_{BIAS} . An accurate overlap of the two saturation curves could then be obtained by relative linear rescaling of both horizontal (MW power) and vertical (EDMR intensity) axis (see also Appendix B). This provides us with a practical correspondence of power scale between the two types of experiment, valid for this specific device mounting, relating a calibrated MW power from the bridge to an I_{BIAS} setting in EDMRoC. Keeping in mind the inhomogeneity of the MW field in the case of EDMRoC, this is to be considered as an effective power scale describing the saturation of the EDMR signal. Indeed, after independent reassembly, a significantly faster saturation behavior can be observed (see Appendix Fig. F1) corresponding to the position of the MOSFET closer to the coil array, demonstrating the sensitivity of the effective power reaching the active layer to this specific distance (see also Appendix Fig. H2).

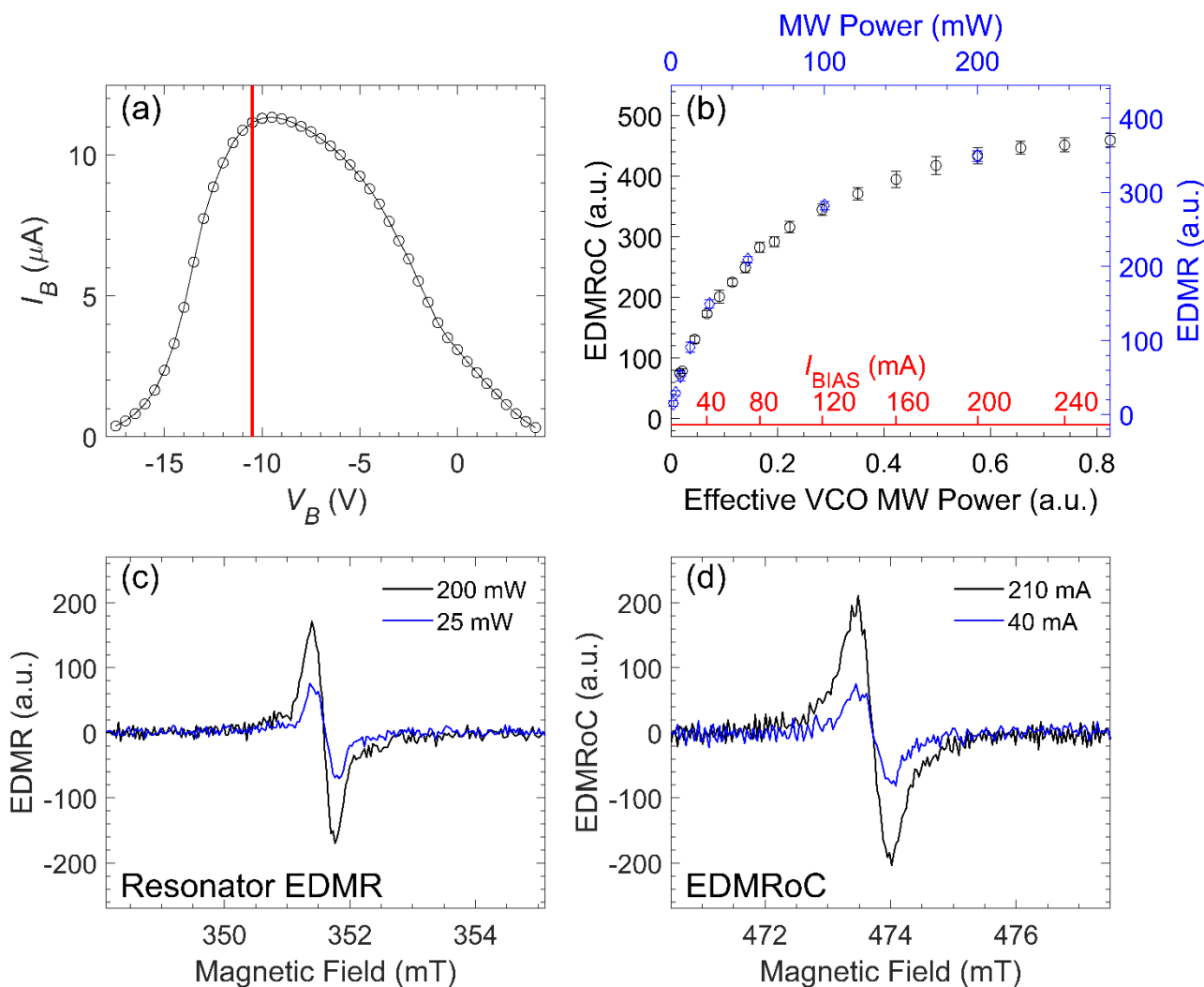


Figure 3: (a) CP current measured at the body contact (I_B) as a function of V_B using $f_{\text{CP}} = 113\text{kHz}$ and $V_A = 10\text{V}$. The red line marks the CP condition used throughout the manuscript. (b) Power dependence of the signal intensity on calibrated power provided by the MW bridge for EDMR in the resonator (blue axes and data points) and on effective power emitted by the VCO for EDMRoC (black axis and data points), as discussed in detail in Appendix A and B. Both abscissa and ordinate are linearly scaled with respect to each other for best mutual fit of the saturation curves. The third abscissa (in red) describes the experimentally applied VCO bias current. The integrated intensities and their error bars are obtained from fitting a normalized simulated EPR signal to the experimental data. (c) EDMR spectra at two distinct MW powers and (d) EDMRoC spectra at two distinct I_{BIAS} settings, to directly compare measured intensities and SNRs at corresponding MW powers. Note that the resonance field is different due to the different MW frequencies (9.85 GHz in panel (c) and 13.28 GHz in panel (d)) and that resonator EDMR is obtained with BM, while EDMRoC is obtained with FM, using similar modulation amplitudes.

Monitoring the CP current during these measurements shows only small changes in the CP current I_{CP} , which increases in absolute value by about 3 % in resonator EDMR as well as in EDMRoC (see Appendix Fig. C1). The change is essentially proportional to MW power and is reversible with a relatively slow response, which points to thermal effects. This is directly



confirmed for the case of EDMRoC by monitoring the Pt1000 sensor on the heat sink of the MW chip, showing an increase in temperature of nearly 20 K over the used I_{BIAS} range (Appendix Fig. C2(a)). Nearly the same increase in I_{CP} is observed under external heating, while the MW chip is not activated (Appendix Fig. C2(b)). Therefore, in EDMRoC the sample warm-up is dominated by transfer of the heat dissipated by the EPR chip, with only limited effect of MW absorption by the sample. On the other hand, for in-resonator EDMR, the entire sample circuitry is embedded in the MWs, and the whole variation in CP current can be attributed to absorption of the MWs by the materials composing the device (ohmic losses in metals and doped semiconductors) and its mounting elements (metallic and polymeric parts of the sample PCB, glue fixing the chip). While this appears unavoidable for in-resonator EDMR, the heating effects can be mitigated in EDMRoC. Indeed, temperature stabilization of the MW chip may be incorporated in future designs, so that only the small effect of the MWs impinging on the active layer remains.

2.2.2. Conventional EDMR versus EDMRoC

Figure 3 compares CP-detected EDMR spectra recorded in the field-swept mode in the same device, either in the resonator configuration with BM (Fig. 3(c)) or in the EDMRoC setup with FM (Fig. 3(d)) for a single scan with total integration time of 3 min, demonstrating that very similar signal intensities and SNRs can be achieved. A SNR of 23.6 (15.6) and 23.4 (8.1) were achieved for conventional EDMR and EDMRoC, for resonator MW powers of 200 mW (25 mW) and I_{BIAS} of 210 mA (40 mA), respectively, in which signal intensity is taken as the maximum of the EDMR signal and the noise as the standard deviation of the signal from the base line outside the resonance. Note that in EDMRoC the noise level is determined by the noise floor of the MW chip, while in resonator EDMR the noise is reduced more or less proportionally with the signal for lower MW power, therefore better SNRs are obtained for EDMRoC with increasing MW power. These SNR comparisons are taken at matching effective power levels, as derived earlier based on the signal saturation behavior in both configurations (see also Appendix A and B).

This comparison is meaningful, as the signals are obtained on the same sample, the as-mounted and bonded device, either inserted in the MW resonator or placed face-to-face on the MW chip, with the same orientation of the static magnetic field relative to the MOSFET plane. Also, experimental parameters were kept identical where possible, in particular the CP conditions, the settings of both the TIA and the EPR signal processing unit, and the parameters of the field sweep; the latter is performed in the same electromagnet. It is true that each approach comes with its own modulation technique, BM for conventional EDMR and FM for EDMRoC, but their respective modulation amplitudes $\Delta\nu$ (6.4 MHz) and ΔB_0 (0.2 mT), smaller than the linewidth, were closely matched according to $\Delta\nu$ (in MHz) $\cong 28.025 \Delta B_0$ (in mT), based on the resonance condition for $g \cong 2$.

It is worth reminding that the resonance occurs at higher magnetic fields in EDMRoC due to the higher MW frequency (13.28GHz) compared to EDMR in the X-band high-Q resonator (9.85GHz). Also, the effects of strain inhomogeneity appear in the linewidth of the resonance (18 MHz in EDMRoC vs. 12 MHz in resonator EDMR), leading to reduced resolution of sidebands as visible in Fig. 3(c) and Fig. 3(d).

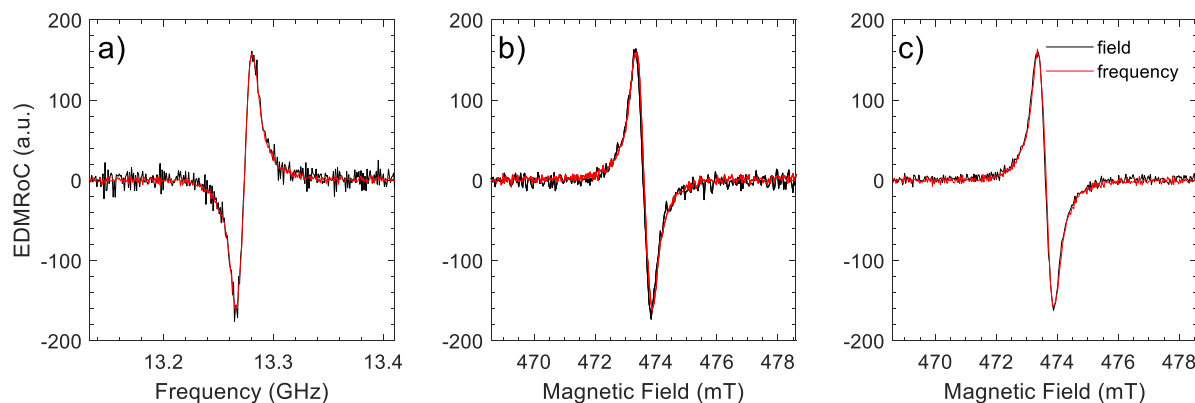


280 Although not obvious from this SNR comparison, FM as modulation technique has an interesting advantage over BM specifically in EDMR. Indeed, the electrical circuitry connecting the MOSFET tends to pick up the alternating field involved in BM, a signal that passes the TIA low-pass filter and the phase-sensitive detection (as it is at the detection frequency) and amplified just like the EDMR signal. BM induces a constant background signal to the measured spectrum, which limits the amplification that can be used at different stages and can also introduce added noise. This is avoided using FM, which is particularly important in weak signal situations.

285 2.2.3. Frequency-swept versus field-swept EDMRoC

Scanning either field or frequency in EDMRoC measurements hardly changes the SNR, as is shown by comparison of the spectra in Fig. 4a and Fig. 4b for which the same sample stayed in the same position in the electromagnet (either at fixed field or scanning, respectively) using the same integration times and corresponding number of points for both spectra. The spectra can be accurately overlapped after appropriate axis transformation of the abscissa, as demonstrated in Fig. 4c.

290



295 **Figure 4:** (a) Frequency-swept EDMRoC spectrum with one (black) or ten (red) scans at an $I_{\text{BIAS}} = 100$ mA. (b) Magnetic-field-swept EDMRoC spectrum with one (black) or ten (red) scans and (c) Comparison of field and frequency-swept EDMRoC spectra (each 10 scans) superimposed by making the conversion: B (mT) = ν (GHz) / 0.028025. Note that going from field to frequency sweeping leads to inversion of the abscissa scale, as low-to-high frequency effectively corresponds to high-to-low magnetic field.

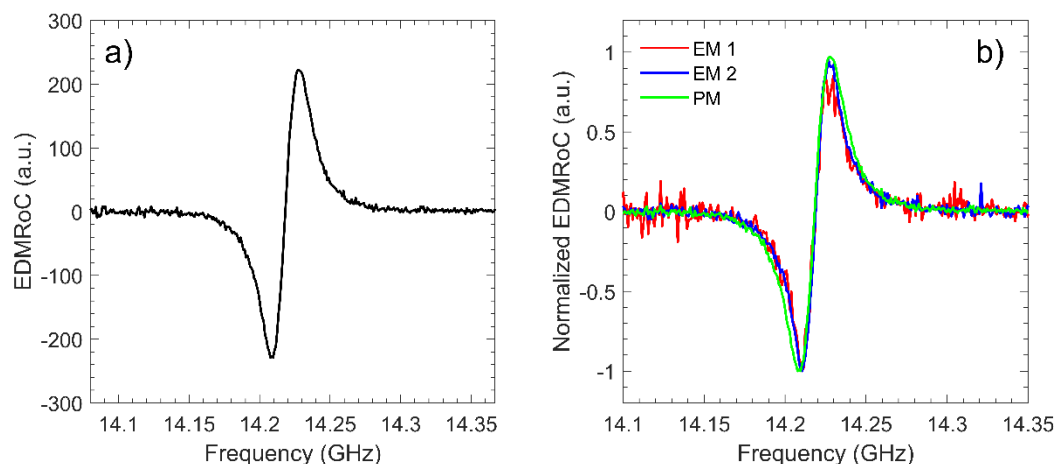
2.3. An ultra-compact EDMRoC Spectrometer

We have demonstrated here SNRs for CP-detected EDMR of a SiC MOSFET in EDMRoC comparable to conventional EDMR, also when scanning the MW frequency instead of the static field and using FM instead of BM for phase-sensitive detection. As previously suggested, (Handwerker et al., 2016; Schlecker et al., 2017; Segantini et al., 2023) the compact EDMRoC MW source can now be combined with permanent magnets replacing the bulky and expensive electromagnet. A

300

simple demonstrator using a pair of cylindrical permanent magnets (NdFeB, $\varnothing 35$ mm \times h20 mm) is shown in Fig. 1c. Here, the magnets are symmetrically installed on both sides of the sample area offering a 17 mm wide gap and delivering a static magnetic field of 507 mT as required for a MW frequency of 14.2 GHz. Straightforward rail mounting allows for relative
305 positioning of sample vs. magnet assembly (see Fig. 1c).

An as-obtained spectrum with integration time of 3 min is presented in Fig. 5 demonstrating that this compact and relatively low-cost set-up essentially allows for the same experiments as described in previous paragraphs. Accurate positioning in the region of lowest inhomogeneity of the static field resulted in spectra with the same linewidth as in the dedicated electromagnet. Interestingly, even better SNRs can be obtained in this simple demonstrator compared to the sweepable
310 electromagnet (Fig. 5(b)), as in the latter there is evidence for pick-up noise induced in the relatively long coax cables (Fig.2(b)) connecting the MOSFET with the CP detection setup. Note that the small line broadening observed for the permanent magnet assembly most likely originates from a slightly more inhomogeneous B_0 field in this very simple design. While this demonstrator evidently calls for further smart design of the magnet/sample set-up (e.g., with better field homogeneity and/or easier access to the sample area) and of other components of the spectrometer, it gives a taste of the
315 possibilities opening up for ultra-compact, low-budget and dedicated EPRoC and EDMRoC spectrometers.



320 **Figure 5: a) Single-scan frequency-swept EDMRoC spectrum ($I_{\text{BIAS}} = 100$ mA) with the external permanent magnet assembly as presented in Fig. 1c providing a magnetic field of 507 mT and thus a resonance MW frequency around 14.2 GHz. b) Comparison of spectra and SNRs in the permanent magnet assembly (PM, in green) and two different measurements with the electromagnet (EM) where the coax cables are either mounted in close proximity of the magnet poles (EM 1, in red) or as far away from them as possible (EM 2, in blue), showing pick-up noise from the electromagnet.**



3. Discussion and Perspectives

325 The quite remarkable performance of CP-detected EDMRoC in terms of signal magnitude and SNR, comparable with
optimized conventional in-resonator EDMR, is a convincing demonstration of its potential for the investigation of
recombination defects in SiC MOSFETs. Moreover, one can foresee wider application of EDMRoC using other detection
modes, *e.g.* via specific diode currents in the MOSFETs, and involving other materials (GaN, organic semiconductors,
metal-halide perovskites, ...) and other devices (solar cells, light-emitting diodes, sensors, ...) in which recombination
330 processes play a central role. In this perspective it is worth considering the limitations and advantages of the method, as well
as possible improvements.

Unlike EDMR in the resonator, there is a stringent requirement of close proximity between the MW chip and device in
EDMRoC. To obtain repeatability of the signal one needs precise control of the relative position of the MW chip and device
and in particular of the distance between them, but this difficulty can be tackled by smart mechanical mounting. At the
335 surface of the MW chip, the orientation of the MW \mathbf{B}_I field is essentially perpendicular to the sample surface, with negligible
in-plane field components $B_{1,x}$ and $B_{1,y}$ (see Appendix Fig. G1, left panel). In this situation the signal would vanish for the
static magnetic field \mathbf{B}_0 perpendicular to the sample surface, as only the component of \mathbf{B}_I perpendicular to \mathbf{B}_0 contributes to
the magnetic resonance transition probability. This at first sight limits the useful range of rotation relative to \mathbf{B}_0 . However, at
a distance above the plane the MW VCOs also induce significant in-plane components $B_{1,x}$ and $B_{1,y}$ in the regions around the
340 coils, comparable in magnitude to $B_{1,z}$ (see Appendix Fig. G1, right panel). This allows detection of EDMR under any
rotation angle of the MW PCB in the external magnetic field. Indeed, the comparison of two mutually perpendicular
orientations of the MW PCB, presented in Fig. H1, shows only a 34% reduction in EDMR intensity for the perpendicular *vs.*
the parallel orientation of \mathbf{B}_0 with respect to the sample surface. The corresponding ratio of transition probabilities was also
calculated using the MW field simulations as a function of distance from the MW PCB surface (see Fig. H2). This ratio
345 starts from zero at the origin, but already reaching 65% at a sample to PCB distance of $z = 15 \mu\text{m}$, in excellent agreement
with the experiment.

Insertion of an EDMR-type sample in a high-Q resonator strongly influences the MW field, typically reducing Q-factor and
SNR, which then sensitively depends on sample position and orientation. In this respect the situation in EDMRoC is much
more robust as it is based on a near-field MW magnetic field emitted by the VCO, operating as a driven oscillator. Also, the
350 number of VCO coils is not restricted to the present 2 rows of 6 coils but can be adapted to the area of the planar sample
under study.

In the evaluation of the saturation behavior of the EDMR signal we already considered the inhomogeneity of the MW field,
as spins probed at different places on the MOSFET experience a different \mathbf{B}_I field. Pulsed EDMR spectroscopy, already
systematically used in resonator configurations, (Akhtar et al., 2015; Behrends et al., 2008; Boehme and Lips, 2003; Harneit
355 et al., 2007; Thomson et al., 2017) ideally requires homogeneity of \mathbf{B}_I to allow for coherent manipulation of the spin motion.
For planar samples, such as solar cells (Segantini et al., 2023) or the present MOSFETs, the implementation of pulse



techniques in EDMRoC is therefore not straightforward. It is well-known that specific MW pulse sequences and pulse shapes can be used to compensate to some extent for B_1 inhomogeneity (Prisner, 2019; Spindler et al., 2016) but the feasibility in the present case needs further investigation.

360 One additional disadvantage of EDMRoC *versus* the in-resonator EDMR approach is that, while the latter can be integrated with a cryostat to perform both low and high temperature experiments, which will be much harder to implement in EDMRoC.

High-Q MW resonators have been systematically applied in EPR spectroscopy to obtain intense MWs in a sample volume but this limits the MWs to a very narrow frequency region, which resulted in the almost general use of magnetic field scanning and modulation (BM). In EDMRoC (as well as in EPRoC), this can be profitably replaced by frequency scanning and modulation (FM), with no loss in signal intensity or SNR as we demonstrated in this work. Specifically in the case of EDMR using FM is advantageous as, contrary to BM, it does not induce background alternating currents in the electronic circuits of the sample. The use of a compact permanent magnet is then a straightforward choice, again with no loss in performance as we have shown in a simple demonstrator. On the contrary, there was a higher noise level using the
370 electromagnet that may be ascribed to the pick-up noise induced by current fluctuations. The absence of a resonator, and the small dimensions of the MW source and sample, also offer perspectives for specialized design of the permanent magnet for different purposes (Alnajjar et al., 2021) such as high homogeneity of the field and/or easy accessibility for sample loading.

4. Conclusions

This successful demonstration of CP-based EDMRoC on a SiC MOSFET opens new perspectives for low-cost and compact
375 EDMR spectrometers for the characterization of recombination processes in electronic microcircuits. The high performance of the set-up, in terms of both signal strength and SNR, indicates that this can be applied in a broad range of materials and devices. As already demonstrated in EPRoC, the MW source can be adapted for different MW frequencies and also on-board preamplification of the signal can be integrated. (Anders et al., 2012; Künstner et al., 2021; Segantini et al., 2023; Yalcin and Boero, 2008) Taking into account the relatively low investment, limited space requirements and versatility in geometry and
380 on-board electronic features, one may envisage table-top spectrometers for specialized research, as well as instruments for quality control either in the lab or even in the production line.



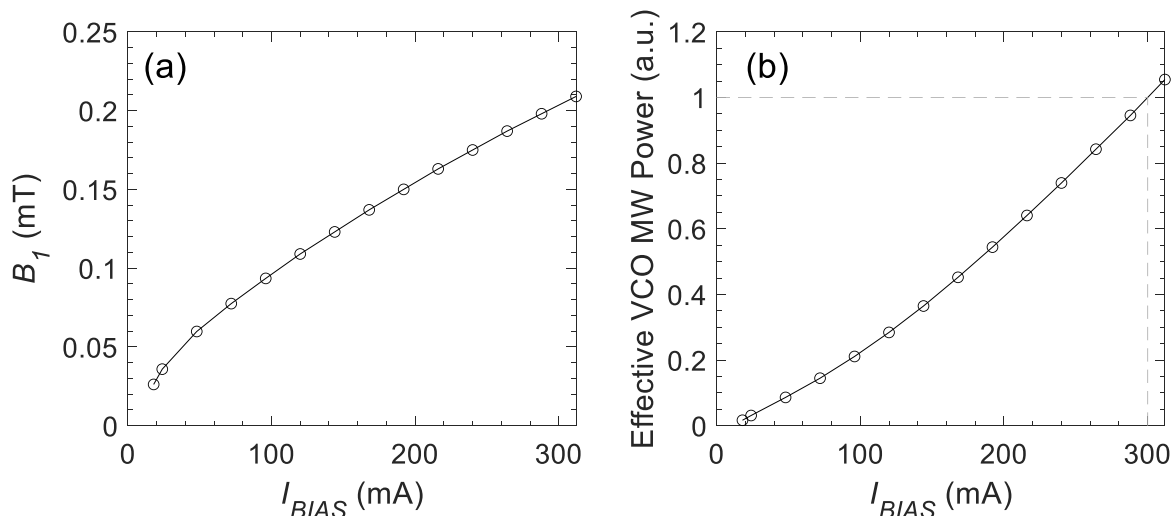
5. Appendices

Appendix A: Microwave power in EDMRoC: dependence on bias current I_{BIAS}

385 Above the threshold current for oscillation, the power emitted by the VCO is smoothly increasing with bias current I_{BIAS} , showing a faster than linear dependence as seen below in Fig. A1. This is derived from an electronic circuit simulation of the ac-current I_{coil} in the coil during oscillation, from which the B_I field magnitude at the coil center (see Fig. A1(a)) can be calculated using the Biot-Savart formula,

$$B_{1,z,\text{Biot-Savart}}(z) = \frac{1}{2} \frac{\mu_0 I_{coil}}{2} \frac{R^2}{(R^2 + z^2)^{3/2}}, \quad (\text{eq. A1})$$

where μ_0 is the vacuum permeability, R the coil radius, z the position along the coil axis taken $z = 0$ in Fig. A1(a). The factor 1/2 takes into consideration that only half the B_1 magnitude is available for MW excitation as only one of the two counter-rotating circularly polarized fields composing the linearly polarized MW field contributes to the magnetic resonance process. The emitted MW power is then proportional to B_I^2 , and rescaled here to 1 for the maximum bias current achievable with this chip, $I_{BIAS} = 300$ mA.



395 **Figure A1:** (a) Dependence on VCO bias current of the B_I field of the MWs and (b) Effective VCO MW power (rescaled to 1 for the maximum $I_{BIAS} = 300$ mA), calculated in the center position in the plane of one of the VCO coils.

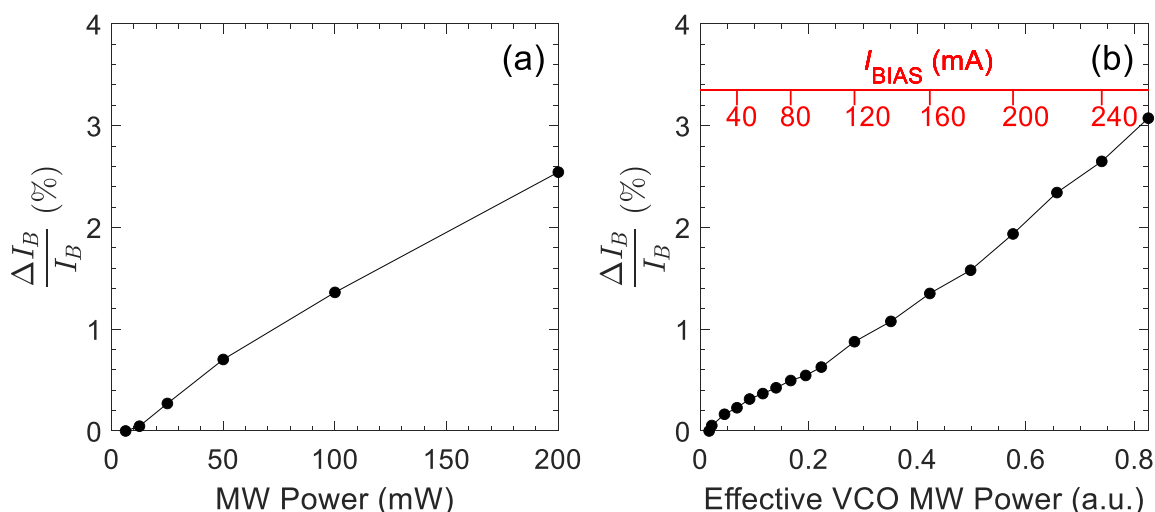
Appendix B: Microwave power in EDMRoC: Scaling relative to resonator EDMR

After linearization of the power scale for the EDMRoC experiment, there is a qualitative correspondence between the saturation curves in both types of experiment. This is clearly demonstrated by **Fig. 3(b)**, obtained by linear relative rescaling on both the horizontal MW power axis (effective scale between 0 and 1 for EDMRoC) and the vertical EDMR intensity axes. The two saturation curves can indeed be nearly perfectly fitted to each other under simultaneous variation of the two

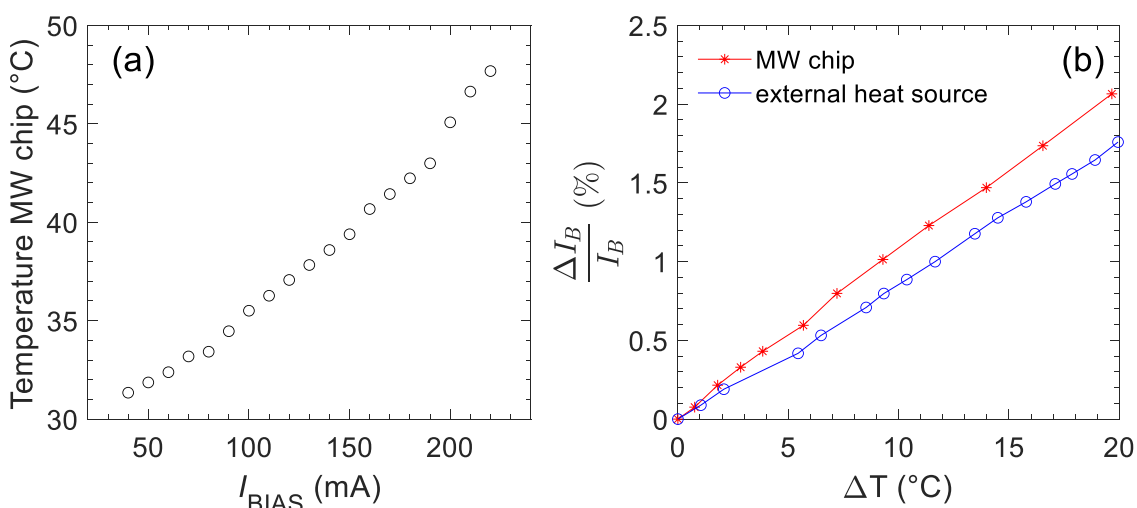


scaling factors. It should be noted that this correspondence is obtained for a specific mounting of the device in EDMRoC and is expected to depend on the distance between MOSFET sample and MW chip surface (see also Fig. F1). We use the
 405 obtained scaling between power delivered by the MW bridge in resonator EDMR with effective MW power in EDMRoC, hence with the bias current I_{BIAS} , to select corresponding spectra for comparison of the SNR (see Fig. 2(c) and Fig. 2(d)): 40 mA \leftrightarrow 25 mW, and 210 mA \leftrightarrow 200mW, for EDMRoC \leftrightarrow resonator EDMR, respectively.

Appendix C: Effect of MW power and temperature on the charge pumping current



410 **Figure C1:** (a) Dependence of the relative change of the CP current on MW power in the resonator and (b) in the EDMRoC configuration. Effective VCO MW power is rescaled according to Fig. A1. The red abscissa gives corresponding values of the bias current I_{BIAS} applied in the experiments.



415 **Figure C2:** (a) Heating of the MW chip as a function of applied I_{BIAS} measured by a Pt1000 sensor attached to the MW chip. (b) Relative change in CP current of the device either heated by an external source (in blue) or heated by the MW chip (in red).



Appendix D: Precise positioning of sample on the MW coil array

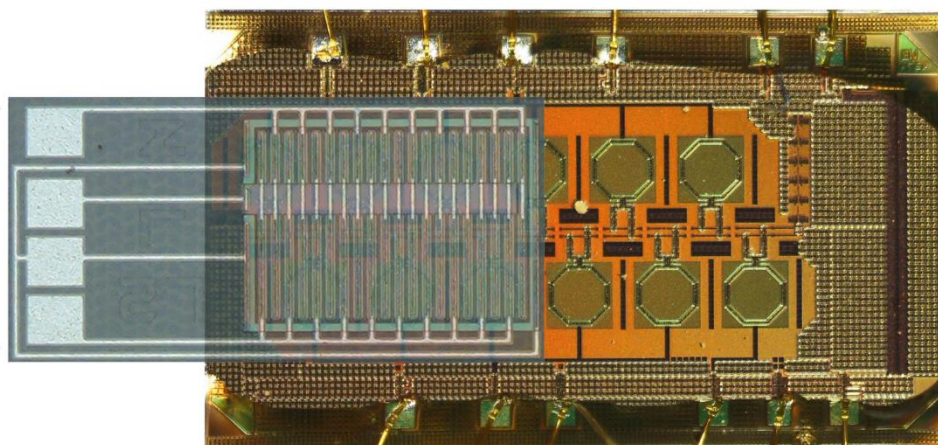


Figure D1: This scheme illustrates the alignment of the MOSFET device onto the VCO coil array, providing an idealized coverage of the MOSFET device by the emission of the VCO coils.

420

Appendix E: Q-factor and conversion of MW power to B_1 in the resonator

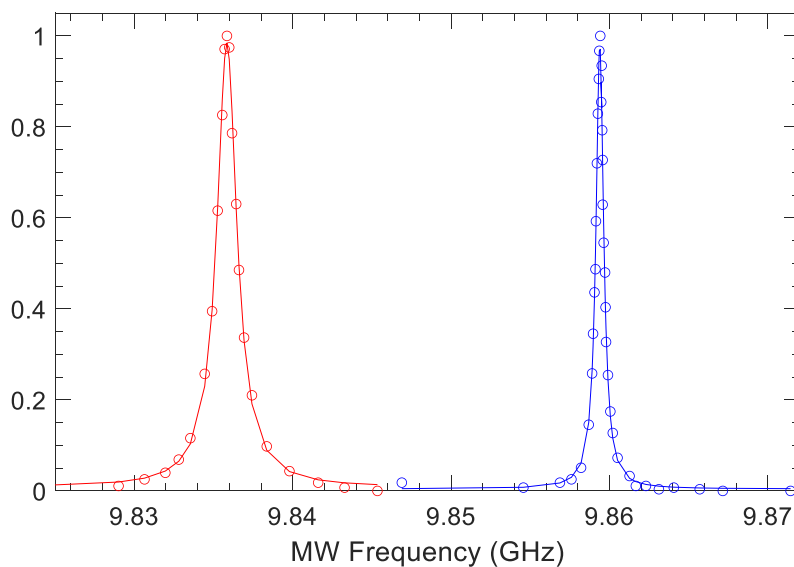


Figure E1: Measurement of the resonance dip of the MWs in the SHQ cylindrical resonator, with estimated $Q = 16700$ for the empty cavity. Loading the resonator with the EDMR sample broadens and shifts the dip and reduces the Q-factor to $Q = 6560$.

425

Based on the relationship $Q = \frac{\nu}{\Delta\nu}$, (Eaton et al., 2010b) with ν the MW frequency and $\Delta\nu$ the FWHM of the dip in the resonator tuning curve, the Q-factor of the empty cavity can be estimated to be $Q_{empty} = \frac{9.859 \text{ GHz}}{0.00059 \text{ GHz}} = 16700$, while the Q-



factor of the loaded resonator amounts to $Q_{loaded} = \frac{9.836 \text{ GHz}}{0.00152 \text{ GHz}} = 6560$. Hence, the resonance broadens significantly, and the Q-factor decreases upon insertion of the MOSFET in the resonator.

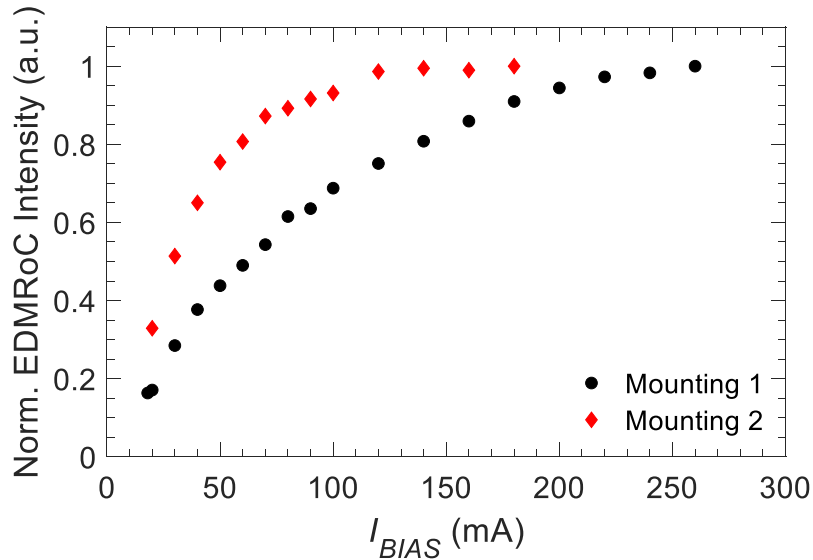
430 The FWHM of the resonator dip for the loaded cavity ($\Delta\nu = 1.5 \text{ MHz}$) and the specific applied MW power, can also be used to calculate the B_I field, given a specific conversion factor C' intrinsic to the used cavity according to (Eaton et al., 2010b):

$$B_1 [\text{mT}] = \frac{C' \sqrt{P[\text{W}]}}{\sqrt{\Delta\nu [\text{MHz}]}} \quad (\text{eq. E1})$$

with $C' = 0.23 [\text{mT MHz}^{\frac{1}{2}} \text{W}^{-\frac{1}{2}}]$ for the ER4122SHQE resonator from Bruker.(Anon, 2024) Using the measured width $\Delta\nu = 1.5 \text{ MHz}$, one calculates $B_I = 30 \text{ } \mu\text{T}$ and $84 \text{ } \mu\text{T}$ on the sample for incident MW powers of 25 mW and 200 mW, respectively.

435

Appendix F: Sensitivity of EDMRoC to specific device mounting



440 **Figure F1: Saturation dependence on I_{BIAS} for two different mountings of the device on the MW chip. The black data points are the ones shown in the main text (Fig. 3(b)), while the red data points indicate a mounting in which the device ended up closer to the MW chip. The red data shows a faster saturation with I_{BIAS} , indicating a higher effective MW power impinging on the MOSFET (see also the z-dependence of transition probabilities in Fig. H2).**

Appendix G: Simulation of the MW field in and above the surface of the MW chip

445 Simulations of the B_1 magnetic field magnitudes were performed with the finite-element simulation software COMSOL Multiphysics. To reduce computational time, the B -field of only one half-coil on an infinite Si substrate in air was simulated at 14 GHz with a coil current of 30 mA. To obtain the B_1 distribution of the complete array, the simulated data of this half-coil were mirrored, translated relative to the first half-coil, superimposed to form a complete coil, and repeated and summed



until forming the entire 12-coil array. In this way, the inductive coupling between the coils is not considered. Further details of the simulation can be found in (Künstner et al., 2024). Figure G1 presents the B_1 -field components in the x, y and z direction of the MW chip, with the z-direction perpendicular to the chip, for two different z positions, in the plane of the
450 MW chip and 25 μm above the MW chip plane.

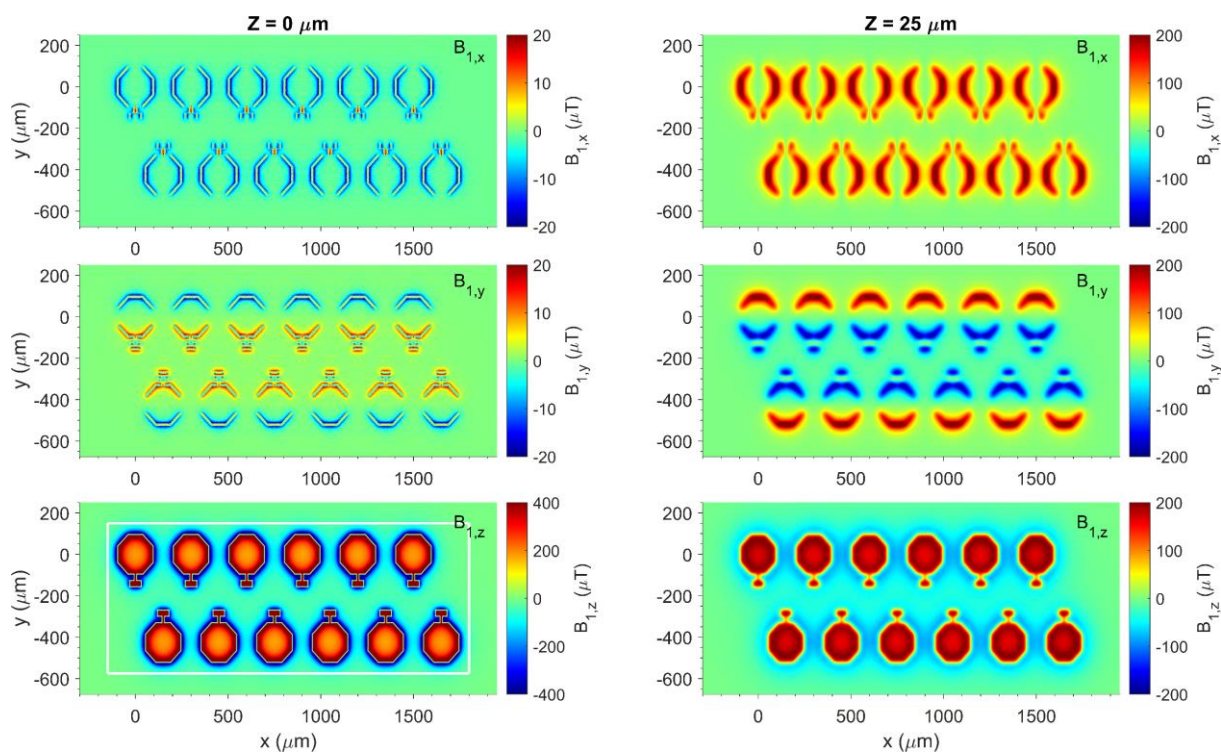


Figure G1: Simulated distribution of the B_1 -field components of the VCO coils at a height of $z = 0$ and $z = 25 \mu\text{m}$ above the surface of the MW chip. Note the different colorbar scales in the different figures.



455 **Appendix H: Angular dependence in EDMRoC**

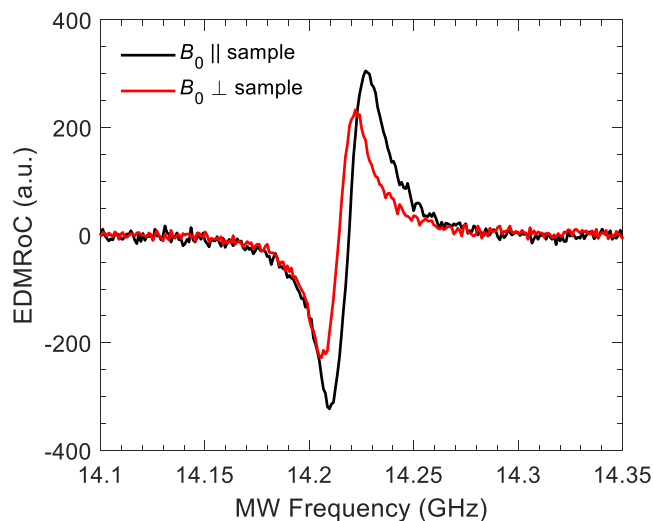
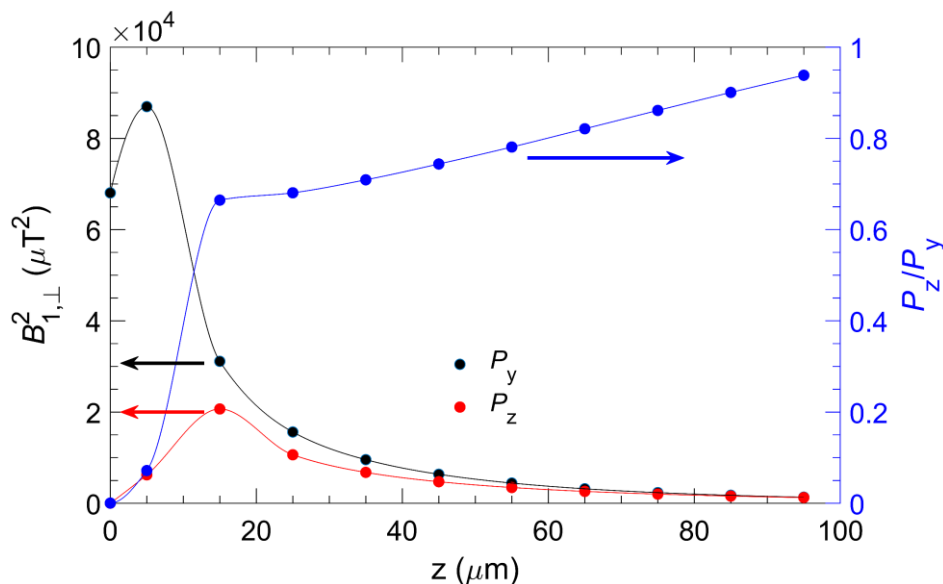


Figure H1: EDMRoC measurements ($I_{\text{BIAS}} = 150$ mA) with the MW PCB mounted either with the sample surface parallel or perpendicular to the external B_0 field of the electromagnet ($B_0 = 507$ mT). Compared to the parallel configuration, the signal in the perpendicular configuration is reduced by only about 34%.



460 Figure H2: Simulations of the mean transition probability, averaged over the white area presented in the bottom left panel of
 Figure G1. This probability is proportional to the squared component of the B_1 field perpendicular to the static field B_0 (i.e.
 465 $P \sim B_{1,\perp}^2$) and is presented as a function of sample mounting distance from the MW chip (z), for the two different orientations
 presented in Figure H1, namely with B_0 parallel to the sample (along the y -axis of the MW chip, $P_y \sim B_{1,x}^2 + B_{1,z}^2$, in black) and
 perpendicular to the sample (along the z -axis of the MW chip, $P_z \sim B_{1,x}^2 + B_{1,y}^2$, in red). The blue data points present the
 calculated ratio between the perpendicular and parallel transition probabilities, which is presented on the right axis of the graph.
 The symbols represent the actual calculations, while a fluent curve is drawn through the data points using a piecewise cubic



Hermite interpolating polynomial. P_y/P_z approaches 0 for small z , due to the negligible $B_{1,x}$ and $B_{1,y}$ in the plane of the MW chip (see Figure G1).

470 **Data availability**

The data that support the findings of this study are available from the corresponding author upon reasonable request.

Author contributions

J.L., S.C., E.G. and I.V. performed the EDMR and EDMRoC experiments and their data analysis. J.L., M.A. and P.M. designed the MOSFET devices with appropriate dimensions for EDMRoC and prepared the bonded MOSFET devices on the
475 sample PCBs. A.C., Ph.H., M.K. and J.A. designed the MW chip and adjusted it for the current EDMRoC experiments. A.C. and M.K. performed the theoretical simulations of the MW emission from the VCOs. J.A. and E.G. conceptualized this work. J.A., P.M., E.G. and S.C. supervised the work. E.G. and S.C. wrote the manuscript, with contributions of all authors.

Competing interests

The authors declare that they have no conflict of interest.

480 **Acknowledgements**

J. L. gratefully acknowledged the financial support of the Flemish Government and Flanders Innovation & Entrepreneurship (VLAIO) through the Baekeland project number HBC.2019.2171. We also acknowledge the fund for scientific research Flanders (FWO-Vlaanderen) for infrastructure funding for the EPR instrumentation (I004920N). MK acknowledges Markus Wick for help with initial setup of the numerical simulations. We also acknowledge funding from the German Research
485 Foundation (DFG) under contract no. AN 984/25-1 and the German Ministry of Research and Education under contract no. 03SF0565C.

References

- Aichinger, T. and Lenahan, P. M.: Giant amplification of spin dependent recombination at heterojunctions through a gate controlled bipolar effect, Appl. Phys. Lett., 101, 083504, <https://doi.org/10.1063/1.4747495>, 2012.
- 490 Aichinger, T., Lenahan, P. M., and Peters, D.: Interface Defects and Negative Bias Temperature Instabilities in 4H-SiC PMOSFETs – A Combined DCIV/SDR Study, Mater. Sci. Forum, 740–742, 529–532, <https://doi.org/10.4028/www.scientific.net/MSF.740-742.529>, 2013.
- Akhtar, W., Schnegg, A., Veber, S., Meier, C., Fehr, M., and Lips, K.: CW and pulsed electrically detected magnetic



- resonance spectroscopy at 263 GHz/12 T on operating amorphous silicon solar cells, *J. Magn. Reson.*, 257, 94–101,
495 <https://doi.org/10.1016/j.jmr.2015.05.012>, 2015.
- Allerstam, F., Ólafsson, H. Ö., Gudjónsson, G., Dochev, D., Sveinbjörnsson, E. Ö., Rödle, T., and Jos, R.: A strong
reduction in the density of near-interface traps at the SiO₂/4H-SiC interface by sodium enhanced oxidation, *J. Appl. Phys.*,
101, 124502, <https://doi.org/10.1063/1.2745321>, 2007.
- Alnajjar, B. M. K., Buchau, A., Baumgärtner, L., and Anders, J.: NMR magnets for portable applications using 3D printed
500 materials, *J. Magn. Reson.*, 326, 106934, <https://doi.org/10.1016/j.jmr.2021.106934>, 2021.
- Anders, J., Angerhofer, A., and Boero, G.: K-band single-chip electron spin resonance detector, *J. Magn. Reson.*, 217, 19–
26, <https://doi.org/10.1016/j.jmr.2012.02.003>, 2012.
- Anders, M. A., Lenahan, P. M., Cochrane, C. J., and van Tol, J.: Physical nature of electrically detected magnetic resonance
through spin dependent trap assisted tunneling in insulators, *J. Appl. Phys.*, 124, 215105, <https://doi.org/10.1063/1.5057354>,
505 2018.
- Anders, M. A., Lenahan, P. M., Harmon, N. J., and Flatté, M. E.: A technique to measure spin-dependent trapping events at
the metal–oxide–semiconductor field-effect transistor interface: Near zero field spin-dependent charge pumping, *J. Appl.*
Phys., 128, 244501, <https://doi.org/10.1063/5.0027214>, 2020.
- Anon: Private communication with Bruker, 2024.
- 510 Ashton, J. P., Lenahan, P. M., Lichtenwalner, D. J., Lelis, A. J., and Anders, M. A.: Electrically detected magnetic resonance
study of barium and nitric oxide treatments of 4H-SiC metal-oxide-semiconductor field-effect transistors, *J. Appl. Phys.*,
126, 145702, <https://doi.org/10.1063/1.5120704>, 2019.
- Bathen, M. E., Lew, C. T.-K., Woerle, J., Dorfer, C., Grossner, U., Castelletto, S., and Johnson, B. C.: Characterization
methods for defects and devices in silicon carbide, *J. Appl. Phys.*, 131, 140903, <https://doi.org/10.1063/5.0077299>, 2022.
- 515 Behrends, J., Schnegg, A., Boehme, C., Haas, S., Stiebig, H., Finger, F., Rech, B., and Lips, K.: Recombination and transport
in microcrystalline pin solar cells studied with pulsed electrically detected magnetic resonance, *J. Non. Cryst. Solids*, 354,
2411–2415, <https://doi.org/10.1016/j.jnoncrsol.2007.09.086>, 2008.
- Bittel, B. C., Lenahan, P. M., Ryan, J. T., Fronheiser, J., and Lelis, A. J.: Spin dependent charge pumping in SiC metal-
oxide-semiconductor field-effect-transistors, *Appl. Phys. Lett.*, 99, 083504, <https://doi.org/10.1063/1.3630024>, 2011.
- 520 Boehme, C. and Lips, K.: Electrical Detection of Spin Coherence in Silicon, *Phys. Rev. Lett.*, 91, 246603,
<https://doi.org/10.1103/PhysRevLett.91.246603>, 2003.
- Boehme, C. and Malissa, H.: Electrically Detected Magnetic Resonance Spectroscopy, in: *eMagRes*, edited by: R.K. Harris,
R. L. W., John Wiley & Sons, Ltd, Chichester, UK, 83–100, <https://doi.org/10.1002/9780470034590.emrstm1525>, 2017.
- Van den bosch, G., Groeseneken, G. V., Heremans, P., and Maes, H. E.: Spectroscopic charge pumping: A new procedure
525 for measuring interface trap distributions on MOS transistors, *IEEE Trans. Electron Devices*, 38, 1820–1831,
<https://doi.org/10.1109/16.119021>, 1991.
- Brugler, J. S. and Jespers, P. G. A.: Charge pumping in MOS devices, *IEEE Trans. Electron Devices*, 16, 297–302,



- <https://doi.org/10.1109/T-ED.1969.16744>, 1969.
- Chu, A., Kern, M., Khan, K., LiPS, K., and Anders, J.: A 263GHz 32-Channel EPR-on-a-Chip Injection-Locked VCO-
530 Array, in: 2023 IEEE International Solid-State Circuits Conference (ISSCC), 20–22,
<https://doi.org/10.1109/ISSCC42615.2023.10067623>, 2023.
- Cochrane, C. J., Bittel, B. C., Lenahan, P. M., Fronheiser, J., Matocha, K., and Lelis, A. J.: EDMR and EPR Studies of 4H
SiC MOSFETs and Capacitors, *Mater. Sci. Forum*, 645–648, 527–530, <https://doi.org/10.4028/www.scientific.net/MSF.645-648.527>, 2010.
- 535 Cochrane, C. J., Lenahan, P. M., and Lelis, A. J.: Identification of a silicon vacancy as an important defect in 4H SiC metal
oxide semiconducting field effect transistor using spin dependent recombination, *Appl. Phys. Lett.*, 100, 023509,
<https://doi.org/10.1063/1.3675857>, 2012.
- Cochrane, C. J., Lenahan, P. M., and Lelis, A. J.: The effect of nitric oxide anneals on silicon vacancies at and very near the
interface of 4H SiC metal oxide semiconducting field effect transistors using electrically detected magnetic resonance, *Appl.*
540 *Phys. Lett.*, 102, 193507, <https://doi.org/10.1063/1.4805355>, 2013.
- Cotton, J., Gruber, G., Pobegen, G., Aichinger, T., and Shluger, A. L.: Recombination defects at the 4H-SiC/SiO₂ interface
investigated with electrically detected magnetic resonance and ab initio calculations, *J. Appl. Phys.*, 124, 045302,
<https://doi.org/10.1063/1.5024608>, 2018.
- Djezzar, B.: Odyssey of the charge pumping technique and its applications from micrometric- to atomic-scale era, *J. Appl.*
545 *Phys.*, 134, 220701, <https://doi.org/10.1063/5.0176246>, 2023.
- Eaton, G. R., Eaton, S. S., Barr, D. P., and Weber, R. T.: Resonator Q, in: *Quantitative EPR*, Springer Vienna, Vienna, 79–
87, https://doi.org/10.1007/978-3-211-92948-3_7, 2010a.
- Eaton, G. R., Eaton, S. S., Barr, D. P., and Weber, R. T.: Resonator Q, in: *Quantitative EPR*, Springer Vienna, Vienna, 79–
87, https://doi.org/10.1007/978-3-211-92948-3_7, 2010b.
- 550 Groeseneken, G., Maes, H. E., Beltran, N., and De Keersmaecker, R. F.: A reliable approach to charge-pumping
measurements in MOS transistors, *IEEE Trans. Electron Devices*, 31, 42–53, <https://doi.org/10.1109/T-ED.1984.21472>,
1984.
- Gruber, G., Hadley, P., Koch, M., and Aichinger, T.: Electrically detected magnetic resonance study of defects created by
hot carrier stress at the SiC/SiO₂ interface of a SiC n -channel metal-oxide-semiconductor field-effect transistor, *Appl. Phys.*
555 *Lett.*, 105, 043506, <https://doi.org/10.1063/1.4891847>, 2014.
- Gruber, G., Cotton, J., Meszaros, R., Koch, M., Pobegen, G., Aichinger, T., Peters, D., and Hadley, P.: Electrically detected
magnetic resonance of carbon dangling bonds at the Si-face 4H-SiC/SiO₂ interface, *J. Appl. Phys.*, 123, 161514,
<https://doi.org/10.1063/1.4985856>, 2018.
- Handwerker, J., Schlecker, B., Wachter, U., Radermacher, P., Ortmanns, M., and Anders, J.: 28.2 A 14GHz battery-operated
560 point-of-care ESR spectrometer based on a 0.13 μ m CMOS ASIC, in: 2016 IEEE International Solid-State Circuits
Conference (ISSCC), 476–477, <https://doi.org/10.1109/ISSCC.2016.7418114>, 2016.



- Harada, S., Kosugi, R., Senzaki, J., Cho, W.-J., Fukuda, K., Arai, K., and Suzuki, S.: Relationship between channel mobility and interface state density in SiC metal–oxide–semiconductor field-effect transistor, *J. Appl. Phys.*, 91, 1568–1571, <https://doi.org/10.1063/1.1428085>, 2002.
- 565 Harneit, W., Boehme, C., Schaefer, S., Huebener, K., Fostiropoulos, K., and Lips, K.: Room Temperature Electrical Detection of Spin Coherence in C60, *Phys. Rev. Lett.*, 98, 216601, <https://doi.org/10.1103/PhysRevLett.98.216601>, 2007.
- Kagoyama, Y., Okamoto, M., Yamasaki, T., Tajima, N., Nara, J., Ohno, T., Yano, H., Harada, S., and Umeda, T.: Anomalous carbon clusters in 4H-SiC/SiO₂ interfaces, *J. Appl. Phys.*, 125, 065302, <https://doi.org/10.1063/1.5066356>, 2019.
- 570 Kaplan, D., Solomon, I., and Mott, N. F.: Explanation of the large spin-dependent recombination effect in semiconductors, *J. Phys. Lettres*, 39, 51–54, <https://doi.org/10.1051/jphyslet:0197800390405100>, 1978.
- Künstner, S., Chu, A., Dinse, K.-P., Schnegg, A., McPeak, J. E., Naydenov, B., Anders, J., and Lips, K.: Rapid-scan electron paramagnetic resonance using an EPR-on-a-Chip sensor, *Magn. Reson.*, 2, 673–687, <https://doi.org/10.5194/mr-2-673-2021>, 2021.
- 575 Künstner, S., McPeak, J. E., Chu, A., Kern, M., Wick, M., Dinse, K. P., Anders, J., Naydenov, B., and Lips, K.: Microwave field mapping for EPR on a Chip experiments, *Sci. Adv.*, accepted, 2024.
- Lepine, D. J.: Spin-Dependent Recombination on Silicon Surface, *Phys. Rev. B*, 6, 436–441, <https://doi.org/10.1103/PhysRevB.6.436>, 1972.
- Letzens, J., Allerstam, F., Franchi, J., Cambré, S., Goovaerts, E., Vrielinck, H., and Moens, P.: Complications of Charge Pumping Analysis for Silicon Carbide MOSFETs, *Mater. Sci. Forum*, 1090, 171–178, <https://doi.org/10.4028/p-84nz7l>, 2023.
- 580 Li, G., Kim, C. H., Lane, P. A., and Shinar, J.: Magnetic resonance studies of tris-(8-hydroxyquinoline) aluminum-based organic light-emitting devices, *Phys. Rev. B*, 69, 165311, <https://doi.org/10.1103/PhysRevB.69.165311>, 2004.
- Malissa, H., Kavand, M., Waters, D. P., van Schooten, K. J., Burn, P. L., Vardeny, Z. V., Saam, B., Lupton, J. M., and
- 585 Boehme, C.: Room-temperature coupling between electrical current and nuclear spins in OLEDs, *Science*, 345, 1487–1490, <https://doi.org/10.1126/science.1255624>, 2014.
- Matheoud, A. V., Gualco, G., Jeong, M., Zivkovic, I., Brugger, J., Rønnow, H. M., Anders, J., and Boero, G.: Single-chip electron spin resonance detectors operating at 50 GHz, 92 GHz, and 146 GHz, *J. Magn. Reson.*, 278, 113–121, <https://doi.org/10.1016/j.jmr.2017.03.013>, 2017.
- 590 McCrory, D. J., Anders, M. A., Ryan, J. T., Shrestha, P. R., Cheung, K. P., Lenahan, P. M., and Campbell, J. P.: Slow- and rapid-scan frequency-swept electrically detected magnetic resonance of MOSFETs with a non-resonant microwave probe within a semiconductor wafer-probing station, *Rev. Sci. Instrum.*, 90, 014708, <https://doi.org/10.1063/1.5053665>, 2019.
- Okamoto, D., Yano, H., Hatayama, T., Uraoka, Y., and Fuyuki, T.: Criteria for Accurate Measurement of Charge-Pumping Current in 4H-SiC MOSFETs, *Mater. Sci. Forum*, 600–603, 747–750, [https://doi.org/10.4028/www.scientific.net/MSF.600-](https://doi.org/10.4028/www.scientific.net/MSF.600-603.747)
- 595 603.747, 2008.



- Prisner, T. F.: Shaping EPR: Phase and amplitude modulated microwave pulses, *J. Magn. Reson.*, 306, 98–101, <https://doi.org/10.1016/j.jmr.2019.07.023>, 2019.
- Rong, F. C., Buchwald, W. R., Poindexter, E. H., Warren, W. L., and Keeble, D. J.: Spin-dependent Shockley-read recombination of electrons and holes in indirect-band-gap semiconductor p-n junction diodes, *Solid. State. Electron.*, 34, 835–841, [https://doi.org/10.1016/0038-1101\(91\)90229-R](https://doi.org/10.1016/0038-1101(91)90229-R), 1991.
- Schlecker, B., Chu, A., Handwerker, J., Kiinstner, S., Ortmanns, M., Lips, K., and Anders, J.: VCO-based ESR-on-a-chip as a tool for low-cost, high-sensitivity point-of-care diagnostics, in: 2017 IEEE SENSORS, 1–3, <https://doi.org/10.1109/ICSENS.2017.8233896>, 2017.
- Segantini, M., Marcozzi, G., Djekic, D., Chu, A., Amkreutz, D., Trinh, C. T., Neubert, S., Stannowski, B., Jacob, K., Rudolph, I., McPeak, J. E., Anders, J., Naydenov, B., and Lips, K.: Electrically Detected Magnetic Resonance on a Chip (EDMRoC) for Analysis of Thin-Film Silicon Photovoltaics, *Magnetochemistry*, 9, 183, <https://doi.org/10.3390/magnetochemistry9070183>, 2023.
- Sometani, M., Nishiya, Y., Kondo, R., Inohana, R., Zeng, H., Hirai, H., Okamoto, D., Matsushita, Y., and Umeda, T.: Energy levels of carbon dangling-bond center (PbC center) at 4H-SiC(0001)/SiO₂ interface, *APL Mater.*, 11, 111119, <https://doi.org/10.1063/5.0171143>, 2023.
- Spindler, P. E., Schöps, P., Bowen, A. M., Endeward, B., and Prisner, T. F.: Shaped Pulses in EPR, in: *eMagRes*, John Wiley & Sons, Ltd, Chichester, UK, 1477–1492, <https://doi.org/10.1002/9780470034590.emrstm1520>, 2016.
- Tedlla, B. Z., Zhu, F., Cox, M., Drijkoningen, J., Manca, J., Koopmans, B., and Goovaerts, E.: Understanding Triplet Formation Pathways in Bulk Heterojunction Polymer:Fullerene Photovoltaic Devices, *Adv. Energy Mater.*, 5, 1401109, <https://doi.org/10.1002/aenm.201401109>, 2015.
- Thomson, S. A. J., Hogg, S. C., Samuel, I. D. W., and Keeble, D. J.: Air exposure induced recombination in PTB7:PC 71 BM solar cells, *J. Mater. Chem. A*, 5, 21926–21935, <https://doi.org/10.1039/C7TA03741D>, 2017.
- Umeda, T., Esaki, K., Kosugi, R., Fukuda, K., Morishita, N., Ohshima, T., and Isoya, J.: Electrically Detected ESR Study of Interface Defects in 4H-SiC Metal-Oxide-Semiconductor Field Effect Transistor, *Mater. Sci. Forum*, 679–680, 370–373, <https://doi.org/10.4028/www.scientific.net/MSF.679-680.370>, 2011.
- Umeda, T., Kim, G.-W., Okuda, T., Sometani, M., Kimoto, T., and Harada, S.: Interface carbon defects at 4H-SiC(0001)/SiO₂ interfaces studied by electron-spin-resonance spectroscopy, *Appl. Phys. Lett.*, 113, 061605, <https://doi.org/10.1063/1.5041059>, 2018.
- Umeda, T., Kagoyama, Y., Tomita, K., Abe, Y., Sometani, M., Okamoto, M., Harada, S., and Hatakeyama, T.: Electrically detected-magnetic-resonance identifications of defects at 4H-SiC(0001⁻)/SiO₂ interfaces with wet oxidation, *Appl. Phys. Lett.*, 115, 151602, <https://doi.org/10.1063/1.5116170>, 2019.
- Wang, R., Huang, Y., Yang, D., and Pi, X.: Impurities and defects in 4H silicon carbide, *Appl. Phys. Lett.*, 122, 180501, <https://doi.org/10.1063/5.0145350>, 2023.
- Yalcin, T. and Boero, G.: Single-chip detector for electron spin resonance spectroscopy, *Rev. Sci. Instrum.*, 79, 094105,

<https://doi.org/10.5194/mr-2024-11>
Preprint. Discussion started: 11 July 2024
© Author(s) 2024. CC BY 4.0 License.



630 <https://doi.org/10.1063/1.2969657>, 2008.